



Numerical modeling of diesel and polyoxymethylene dimethyl ether spray in a high pressure chamber using the fischer primary breakup model

Tim Beutler¹ · Niklas Prchal¹ · Michael Günthner¹

Received: 25 October 2021 / Accepted: 13 September 2022 / Published online: 29 October 2022
© The Author(s) 2022

Abstract

In the strive for the climate-neutral and ultra-low emission vehicle powertrains of the future, synthetic fuels produced from renewable sources will play a major role. Polyoxymethylene dimethyl ethers (POMDME or “OME”) produced from renewable hydrogen are a very promising candidate for zero-impact emissions in future CI engines. To optimize the utilisation of these fuels in terms of efficiency, performance and emissions, it is not only necessary to adapt the combustion parameters, but especially to optimize the injection and mixture formation process. In the present work, the spray break-up behavior and mixture formation of OME fuel is investigated numerically in 3D CFD and validated against experimental data from optical measurements in a high pressure/high temperature chamber using Schlieren and Mie scattering. For comparison, the same operating points using conventional diesel fuel were measured in the optical chamber, and the CFD modeling was optimized based on these data. To model the spray-breakup phenomena reliably, the primary break-up model according to Fischer is used, taking into account the nozzle internal flow in a detailed calculation of the disperse droplet phase. As OME has not yet been investigated very intensively with respect to its chemico-physical properties, chemical analyses of the substance properties were carried out to capture the most important parameters correctly in the simulation. With this approach, the results of the optical spray measurement could be reproduced well by the numerical model for the cases studied here, laying the basis for further numerical studies of OME sprays, including real engine operation.

Keywords Numerical spray modeling · Diesel · Polyoxymethylene dimethyl ether · Fischer primary breakup model · Optical spraymeasurement

1 Introduction

Limiting the effects of climate change is one of the most important challenges of this century. Global warming can be attributed directly to anthropogenic greenhouse gases, such as carbon dioxide (CO₂), and thus also to the use of fossil fuels. Current research on vehicle propulsion systems—and internal combustion engines in particular—is, therefore, aiming at both reducing carbon dioxide emissions and exhaust pollutants. In addition to the optimization of engine efficiency, suitable new

fuels need to be identified, as the potential for reducing emissions is limited as long as fossil fuels are used. The use of synthetic and potentially CO₂-neutral fuels, such as POMDME (polyoxymethylene dimethyl ether, or OME for short, which will be used in the following) in diesel engines represents a promising approach for eliminating the current disadvantage of fossil fuels in terms of CO₂ emissions. Synthetic fuels can have a positive impact on the CO₂ balance if they are produced sustainably from renewable sources. Several studies have already demonstrated the potential of pure OME and OME blends under a wide range of operating conditions in commercial vehicle and passenger car engines in terms of emissions and also increased efficiency [1–4]. Due to the molecular composition of oxymethylene ethers— $CH_3O(-CH_2O)_nCH_3$ —and the associated high oxygen content, virtually soot-free combustion and thus an optimization of the soot-NO_x trade-off (i.e., the mutual dependence of soot and NO_x emissions) is possible when pure OME is used without an additional blend

✉ Tim Beutler
tim.beutler@mv.uni-kl.de

✉ Niklas Prchal
niklas.prchal@mv.uni-kl.de

¹ Institute of Vehicle Propulsion Systems (LAF), University of Kaiserslautern (TUK), 67663 Kaiserslautern, Germany

component [5–7]. As a consequence, nitrogen oxide emissions can also be reduced significantly [8]. However, there is a need for further research, especially with regard to the optimization of engine operation. Due to improved evaporation and mixture formation of OME and its higher cetane number, the processes associated with auto-ignition and combustion also differ from diesel fuel [3]. Therefore, besides the effects of modified hydraulic flow of the injectors, also jet break-up behavior, fuel evaporation and mixture formation play a major role in optimizing the combustion process.

The use of 3D computational fluid dynamics (CFD) simulation is a common approach for predicting in-cylinder flow, injection and combustion. The use of a CFD model to simulate the injection process will also be useful for a deeper understanding of the spray break-up behaviour, and for optimising the combustion system for OME. In particular, the simulation of combustion using chemical reaction mechanisms requires a well-validated injection model to provide reliable input data for the subsequent simulation of combustion. This is particularly relevant due to the heterogeneous nature of the in-cylinder mixture in diesel-like combustion processes. In this study, simulations were performed to investigate the spray formation in a constant volume chamber under high pressure and high temperature boundary conditions. In an experimental study, the spray formation was observed using Schlieren and Mie scattering visualization methods. These optical recordings were used to distinguish the liquid from the vapour phase of the spray and to adjust the simulation model constants at different operating points. The investigations were carried out within the framework of the project “E2Fuels” funded by the German Federal Ministry of Economic Affairs and Climate Action. As OME has not yet been investigated very intensively with respect to its chemico-physical properties, chemical analyses of the substance properties were carried out in order to capture the most important parameters correctly in the simulation. With this approach, the results of the optical spray measurement could be reproduced well by the numerical model for the cases studied here, laying the basis for further numerical studies of OME sprays, including real engine operation. The objective of the corresponding project part is the optimization of the combustion process of a passenger car CI engine operating on various synthetic fuels and fuel blends (particularly hydrogenated vegetable oil—HVO, OME and blends of these two fuels) instead of diesel fuel. For this purpose, investigations were carried out on both a single-cylinder research engine and a 6-cylinder engine, which were operated with the different synthetic fuel blends [8]. In order to analyze the corresponding design variants of the injection system, CFD calculations were carried out and compared with experimental data from the optical investigations. These optical reference experiments were conducted externally on a subcontract basis.

Table 1 Temperature-independent physical properties of the studied oxymethylene ether fuel and EN 590 diesel [5, 11–13]

Properties	Unit	Diesel B7	OME3–5
Molecular weight	g/mol	–	136.2–196.2
Density	kg/m ³	820.0–845.0*	1067.0*
Oxygen content	m-%	0.75–0.80	40.9
Boiling point	° C	170–390	156–242
Cetane number	–	>51.0	71.4
Lower heating value	MJ/l	35 - 36	20.7
Diesel equivalent	–	1	1.7
Stoichiometric air–fuel ratio**	kg/kg	14.5	6.09–5.64

* A 15° C

** Calculated

2 Theoretical basics and model setup

OME is the abbreviation for oligomeric polyoxymethylene dimethyl ether and covers all substances with the structural formula $CH_3O(-CH_2O-)_nCH_3$. The fact that like conventional diesel, OME fuels are in liquid state at ambient temperature simplifies integration into the existing infrastructure. In addition to its good environmental compatibility (biodegradability, non-toxicity), directly-injected OME fuel is characterized by good mixture formation and soot-free combustion without particle formation. This results from the oxygen bridges which connect all C-atoms in the molecule through an oxygen atom, thus avoiding direct C–C bonds which otherwise contribute significantly to the formation of soot. Oxymethylene ethers, therefore, exhibit a high oxygen content in the molecule [5, 9, 10].

OME fuels are produced through synthesis processes starting from methanol, which in turn can be produced via sustainable pathways from CO₂ (or CO) and H₂. The production of oxymethylene ethers through both economically viable and ecologically sustainable procedures is currently the subject of numerous research and development activities [3, 11].

For characterization and comparison of OME with diesel, Table 1 shows the properties of diesel according to EN 590, OME1 and OME3–5. The temperature-dependent material data required for the simulation were determined in scientific laboratory tests and are listed in Appendix C. It can be seen that the physical properties of OME depend on their chain length. The low boiling temperature of 42° C and the associated volatility of OME1 might cause problems for in-vehicle storage, and also for blending with diesel. OME3–5—with a boiling temperature very similar to diesel—are much better suited for usage as pure fuels or in blends. Another positive aspect of OME is the increased cetane number. Nevertheless, most fundamental investigations so far have been carried out

Table 2 Parameter variations of the optical data used as reference

Parameters	Variations
Fuel	Diesel, OME3–5 (OME)
Cchamber pressure	50 bar, 65 bar, 80 bar
Chamber temperature	600° C, 650° C, 700° C
Injection pressure	500 bar, 1000 bar, 1500 bar
Injector	8-hole standard common rail solenoid injector designed for diesel fuel

using OME1. A crucial difference between the OME fuels and diesel can be noted in the energy content. Oxymethylene ethers have a 40–50% lower heating value than diesel due to the high oxygen content. Conversely, more OME fuel needs to be injected into the combustion chamber to replace the amount of diesel fuel with the same energy content. Since OME also has a lower oxygen requirement for combustion, the power density of a comparable diesel engine can still be achieved [5, 9, 10].

2.1 Optical measurements

To get an overview of how the spray of the various fuels used in the study differs, experimental measurements in a high temperature/high pressure vessel were carried out. These investigations were subcontracted to Erlangen University and have not been published to date. However, the experimental setup and methodology applied are identical to similar investigations of the same institution [14]. In addition to the fuel, the actuation time, chamber pressure and temperature, as well as the injection pressure were investigated for three different injectors which differ in number of holes and hydraulic flow rate. Table 2 lists the relevant parameters and their variations for this paper. The operating points were chosen to allow an optimal characterization of the spray behavior of the different injectors. For this reason, the activation duration was also kept constant and not adapted to the corresponding energy content of the fuel. This results in a constant pulse input for the respective injectors and thus makes a direct comparison of the fuels and injectors possible. It still needs to be kept in mind that if the same injector is used for OME as for diesel, the actuation time will be almost doubled for the same energy input. However, this is a different discussions, as it is expected that the hydraulic flow rate of the injector will be adapted for engine concepts operating on pure OME. Besides the inert measurements used in this paper to adjust the simulation, also reactive measurements were performed which will subsequently be used to validate the combustion simulation. These experimental data, together with the results from the simulations, are intended to provide information about the combustion

process and serve to optimize the single- and multi-cylinder engine operation on the test bench at the institute.

2.2 Spray model

Fuel injection and the associated droplet break-up and evaporation in an internal combustion engine are based on complicated physical phenomena. Spray characteristics depend on fuel properties, ambient conditions (temperature, pressure, density), injector design and operating conditions. The specific models used to simulate the spray break-up behaviour of diesel and OME are described below. The CFD code used for the simulations discussed in this paper was *AVL FIRETM*.

2.2.1 Spray statistics and Lagrangian spray model

For simulating the injection process, the dispersed multiphase flow produced by the injection event needs to be modeled. Due to the high volume fraction of the continuous gas phase in the combustion chamber in comparison with the dispersed droplet phase, these two regimes have to be described in a fundamentally different manners. The gas phase is described by the continuum mechanic RANS equations and the *k-zeta-f turbulence model* at a macroscopic level, and solved numerically by discretisation methods. This model has proven to be stable and reliable in the past in combination with the 3-Zone Extended Coherent Flame Model (Ecfm3z) [15] which will also be used in the combustion calculations to be performed in the next step of the study.

This continuum flow is a model representation, since in reality there is a continuous molecular motion. With a sufficiently large number of molecules, the stochastic fluctuations have no more influence on the macroscopic flow, and the assumption of a continuum is justified. Accordingly, the macroscopic flow parameters (velocity, pressure, etc.) are mean values of the microscopic quantities [16].

The continuous phase of the injector nozzle internal flow can be calculated in analogy to the gas phase. In the present work, the results of a nozzle internal flow simulation are used as boundary conditions for the spray simulation at the nozzle orifice, so that the setup of the simulation models is reduced to the description of mixture formation in the combustion chamber.

Since the dispersed phase consists of several million droplets with average diameters in the order of a few microns, solving the conservation equations of each droplet and coupling them vice versa is not practical due to computational time constraints. Based on the microscopic observation (i.e., molecular dynamics) of the injection jet, the droplet behavior can be described statistically and with

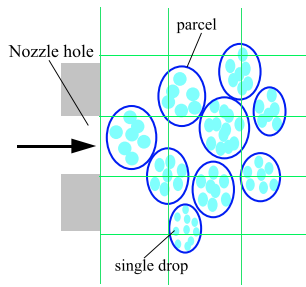


Fig. 1 Schematic diagram of the discrete droplet model (DDM)

additional models. Instead of each individual droplet, a distribution density function is introduced, specifying how many fluid particles N will assume a certain state (described by droplet velocity \mathbf{v}_{Tr} , location $\mathbf{x}_{Tr} = (x, y, z)$, droplet radius r_{Tr} , droplet temperature T_{Tr}) in a volume element at a defined point in time [16, 17]:

$$f(\mathbf{x}_{Tr}, \mathbf{v}_{Tr}, r_{Tr}, T_{Tr}, t) = \frac{dN}{d\mathbf{x}_{Tr} \cdot d\mathbf{v}_{Tr} \cdot dr_{Tr} \cdot dT_{Tr}}$$

With a known distribution density function, all macroscopic flow quantities can be derived in analogy to molecular gas dynamics. A balance equation of the distribution density function—the so-called spray equation—is used to describe the spray dynamics [16, 17].

In the present paper, the numerical solution of the spray equation is based on the Discrete Droplet Model (DDM). In this process, representative particles (the so-called “*parcels*”) are introduced, representing groups of real droplets with the same properties. These particles map the distribution density function at discrete points, so that a solution of the spray equation can be computed. For illustration, this discretization is shown in Fig. 1.

2.2.2 Modelling of the spray breakup

For each parcel introduced into the computational domain, differential equations are solved to describe the trajectory, conservation of momentum, heat transfer, and mass transport. Especially for the spray breakup, the evaporation and the occurring turbulence as well as the momentum exchange with the gas phase, a large number of models are already available for use in CFD calculations. Due to the relative motion between the gas phase and the fuel droplets, drag forces counteract the droplet motion. In addition to drag, pressure forces, gravity, inertial forces, and other external forces cause a change in momentum. The drag force is proportional to the gas density, the effective droplet surface, the square of the velocity as well as the drag coefficient. The standard model according to **Schiller and Naumann** as implemented in *AVL FIRETM* is used in this paper to

calculate the droplet resistance [18]. For simulating diesel injection, the **Dukowicz model** as described in [19] is employed. The fuel used in the OME simulation studies is composed of 60% OME3 and 40% OME4. As the standard Dukowicz model is only suitable for single-component fuels, the **multi-component model** according to [20] and [21] will be used in this case. This evaporation model is based on the **Abramzon-Sirignano** [22] approach and has been extended by **Brenn et al** [23]. Mass transfer is considered separately for each fluid component, but heat transfer is modeled by a global mechanism. A homogeneous fluid composition within a droplet is assumed. A detailed description of the models is not included here. Further information can be found in [23] and [24].

The primary break-up of the fuel droplets is a main focus of this work, since especially the transition from the nozzle internal flow to the dispersed droplet phase is often only mapped very inadequately. One reason why the transition between the effects of the nozzle internal flow and the combustion chamber is not taken into account is the large difference in length scale, which—beside additional factors—would require a very fine computational grid and thus lead to large computing times. Typically, the local flow properties at the nozzle orifice are not taken into account at all, or nozzle effects such as turbulence or cavitation are only implemented via correction factors. By default, a particle size distribution at the nozzle hole exit is specified in addition to the injection rate.

In the following investigation, the **Fischer Primary Break-up Model** is used for the spray matching between the optical measurements and the simulation of the injection. In addition to this model, there are other models available which take into account the local flow fields at the nozzle exit in a Lagrangian approach [25]. The model developed by F. Fischer [26, 27], however, allows a particularly detailed modeling of the near nozzle region. For the application of this model, a simulation of the injector internal flow needs to be carried out previously, so that the flow conditions at the nozzle orifice are available.

For this purpose, the injector geometry is meshed and initialized with the appropriate pressures and temperatures. The different pressure ratios in the injector and in the combustion chamber result in a fuel mass flow which enters the chamber and vaporizes. In Appendix A, some results of a generic nozzle flow simulation are given as an example. The application of the Fischer model is preceded by the setup of a *nozzle file* containing the variables for each time step and each cell of the nozzle hole exit. Additional information can be found in Appendix B. The local flow properties are then transferred to an auxiliary polar grid. For the transition from the continuous flow in the injector to the dispersed droplet spray, the averaged conservation equations for mass and momentum are solved based on the auxiliary grid, as well

as an adapted **k-epsilon turbulence model** for a single-fluid model. In this *sub-model*, the liquid and gaseous phases of the fuel are combined into a fluid with averaged properties [26]. Solving these equations yields the initial breakup of the liquid in the core of the fuel jet. In the next step, the flow field calculated in the single-fluid model is applied to the dispersed fuel droplets. In this process, depending on the fuel mass distribution calculated in the *sub-model*, the *primary blobs* are initialized and their position is varied until the fuel droplets represent the fluid properties. The detachment of the *secondary droplets* is based on the assumption that turbulent fluctuations lead to a perturbation of the fluid surface and the formation of ligaments. Here, the magnitude of these ligaments is due to the size of the local turbulent eddies. After the ligaments reach their critical length at a certain time step, one or more dispersed droplets are formed. The droplet break-up in this case is based either on the *Rayleigh* mechanism or on aerodynamic break-up [26] the latter being more likely in the present case due to the high flow velocities.

Typically, the breakup process cannot be described entirely by a single model, which also applies to the current case. Hence, in this paper, the **Kelvin-Helmholtz/ Rayleigh-Taylor hybrid breakup model** was implemented to simulate the secondary breakup [28]. Since this is usually considered to be better known than the primary breakup, it is common to use this model.

2.3 Modelling the constant volume high pressure chamber and provision of substance data

For the numerical modeling of the injection, the high-pressure chamber used for the optical measurements is discretised. The chamber contours can be reduced to a cylinder. In the center, the external contour of the injection nozzle (i.e., the injector tip) must be taken into account. To reduce the computation time, only one cone of the fuel spray is considered, so that a sector model can be used for the simulation instead of a model of the entire chamber. It is assumed that there are no flow inhomogeneities at the different nozzle holes.

The discretisation of the volume is done by polyhedral grid elements (see Fig. 2), since these are also well-established for engine process simulation. Various mesh studies and test simulations were performed to determine and evaluate the correct cell size. To achieve a better resolution of the jet core and the area near the nozzle, the high-pressure chamber was discretised more finely in these regions by means of a “*cone refinement*” along the jet axis. The computational mesh used in the present simulation is shown in Fig. 2, with the detailed mesh specifications listed in Table 3.

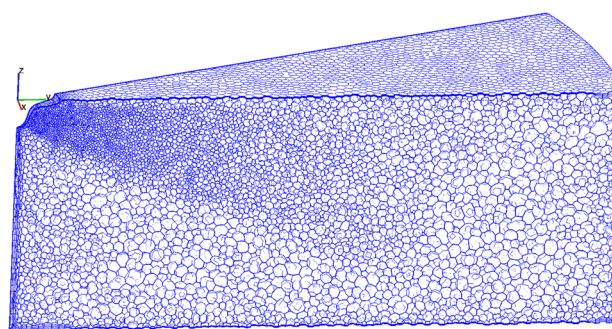


Fig. 2 Computational mesh in the sector of one injector (45°) for the spray injection simulation studies

Table 3 Computational mesh specifications

Parameter	Value
Global mesh size	0.45 mm
Refinement mesh size	0.05 mm
Growth rate	1.04
Boundary layers	3
Discretization	Polyhedral
Overall cells	417873

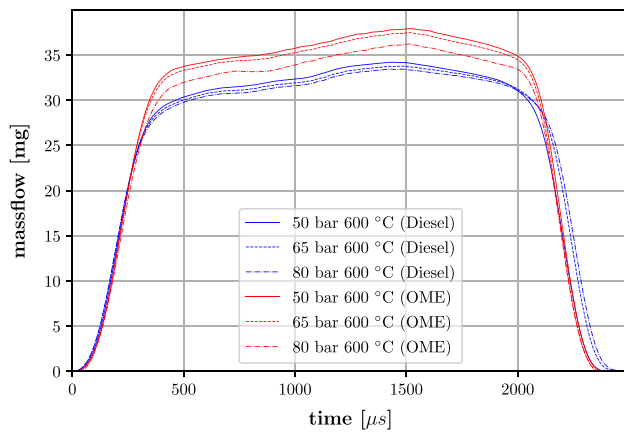
Table 4 Injection system specifications and boundary conditions

Component/parameter	Characterization
Injection system	Common rail system
Injector	Magnetic valve injector
Injector actuation duration	1 ms
Spray pattern	8 cones
Diameter pressure chamber	100 mm
Fuel temperature	90 ° C
Rail pressure	1000 bar

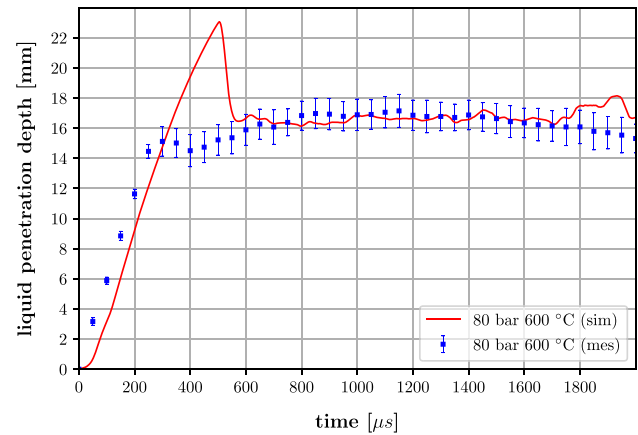
For the experimental studies, an 8-hole standard common rail solenoid injector designed for diesel fuel was installed in the high-pressure chamber. In both measurements and simulation, the injector actuation duration was kept constant at 1 ms, and the fuel was conditioned to 90 ° C like in the measurements, cf. Table 4. The initial conditions need to be chosen depending on the operating point and are listed in Table 5. The resulting mass flow rates are shown in Fig. 3 and demonstrate the significant differences in the flow behavior of the two fuels.

Table 5 Initial conditions for chamber pressure temperature and density

Case	Pressure [bar]	Temperature [°C]	Density [$\frac{kg}{m^3}$]
1	50	600	19.285
2	50	650	18.241
3	50	700	17.303
4	65	600	25.077
5	80	600	30.856

**Fig. 3** Mass flow rates of diesel and OME for different initial conditions**Table 6** Temperature-dependent physical properties of OME3 und OME4

Properties	Unit	Comment
Density (liquid phase)	kg/m ³	Fluid analysis cf. App. C
Dynamic viscosity (liquid phase)	kg/(m*s)	Fluid analysis cf. App. C
Specific heat capacity (liquid phase)	J/(kg*K)	Fluid analysis cf. App. C
Surface tension	N/m	Yaws [29]
Thermal conductivity (liquid phase)	W/(m*K)	Fluid analysis cf. App. C
Evaporation enthalpy	J/kg	Fechter et al. [30]
Vapour pressure	Pa	Fechter et al. [30]
Dynamic viscosity (vapor phase)	kg/(m*s)	Cai et al. [1]
Specific heat capacity (vapor phase)	J/(kg*K)	Cai et al. [1]
Thermal conductivity (vapor phase)	W/(m*K)	Cai et al. [1]

**Fig. 4** Liquid penetration depth of diesel (simulated vs. measured)

In the simulation tool used, temperature-dependent material data is implemented as user input and employed to model the evaporation and breakup behavior. These values were derived either from literature—as far as available—or from a dedicated fuel analysis based on the fuel components used in the experiments. The material properties and their respective source are listed in Table 6. The results of the fluid analysis are included in Appendix C.

3 Results and discussion

For optimizing and validating the numerical modeling of the mixture formation for real injection events, spray visualization measurements, e.g., from a high-pressure chamber operated at realistic conditions are a very valuable tool. For the present investigations, such measurements have been carried out using boundary conditions derived from real engine operating points. The boundary conditions chosen are listed in Table 5. During these measurements, the liquid and the vapor phase were measured simultaneously. These experiments show that while the gas phase continues to penetrate further into the chamber with increasing time after the start of injection and thus describes the tip of the fuel jet, the liquid penetration depth reaches a maximum after a certain injection time. This means that once a certain penetration depth corresponding to the maximum liquid penetration is reached, the evaporation rate is equal to the injection rate (which is kept constant), so that the fuel droplets evaporate but do not penetrate further into the chamber. Thus, the liquid penetration length is characterizing the break-up rate of the jet. The droplet break-up controls the penetration depth, as well as the spray width and the evaporation.

In the following, the penetration depths of the liquid and gaseous phases are compared for the previously listed different operating points. Furthermore, the spray images from the

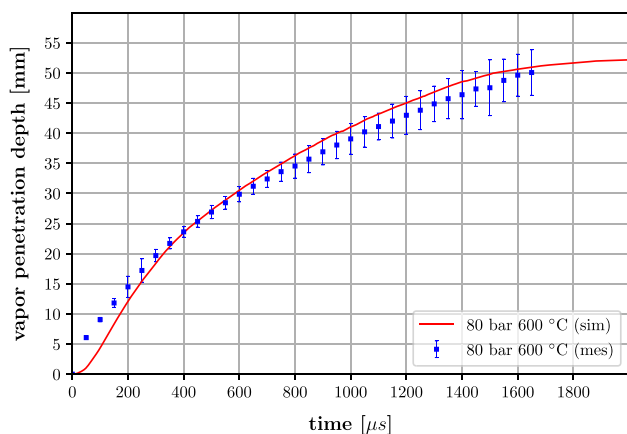


Fig. 5 Vapor penetration depth of diesel (simulated vs. measured)

simulation are superimposed with the optical images taken in the high-pressure chamber, so that a visual comparison is also possible. First, the results for diesel will be presented, followed by the discussion of the OME spray simulation.

3.1 Comparison of diesel spray penetration depths

In Figs. 4 and 5, the simulated liquid and vapor penetration curves as well as the measured liquid and vapor penetration lengths are displayed as a function of time after SOI for the case of 80 bar chamber pressure and 600 °C chamber temperature.

In the simulation, the liquid penetration depth shows an overshoot at the end of the first injection phase before the characteristic penetration depth is reached at which the injection rate and the evaporation rate are in equilibrium. Simulations at other operating points also show a similar slight overshoot. This behaviour could be caused by the calculation method on which the evaluation is based. Dispersed droplets also contribute to the penetration depth of the liquid phase. In the experiments, an intensity threshold value must be determined to calculate the penetration depth. Similarly, such a threshold value is also determined in the simulation results. Here, the liquid penetration depth is defined as the mass-averaged distance of the 1% droplets dispersed farthest from the center of the nozzle hole.

Furthermore, especially the near nozzle area and the mechanisms during the needle opening phase are very difficult to describe correctly with respect to the underlying physics, so that a deviating formation of the fuel spray could also lead to the observed behaviour. In particular, the graphic evaluation of the simulation results shows an accumulation of droplets at the spray tip during the first phase of the injection, disappearing after approx. 500 μs .

Nevertheless, the liquid penetration depths in the simulation occurring after approx. 600 μs agree well with the

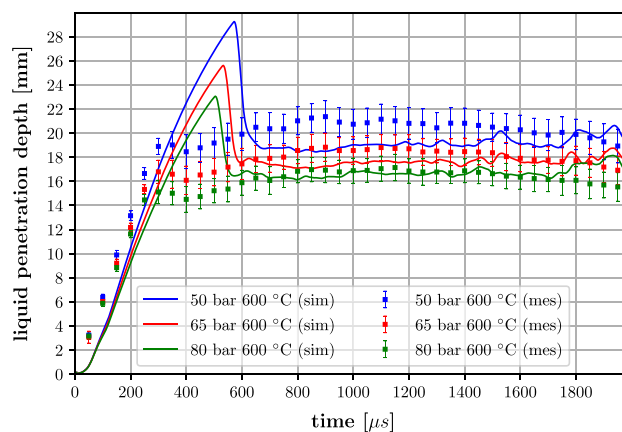


Fig. 6 Liquid penetration depth of diesel for different chamber pressures (simulated vs. measured)

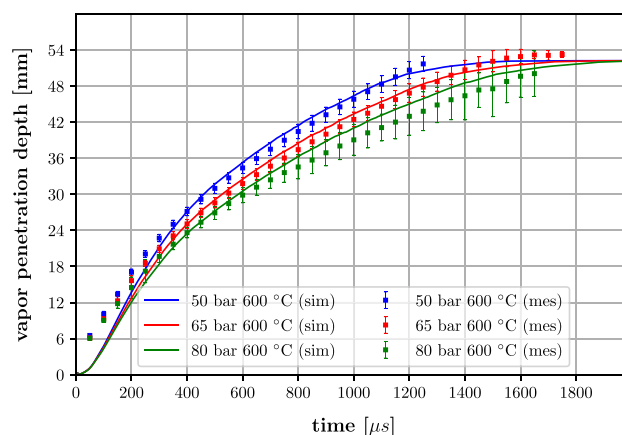


Fig. 7 Vapor penetration depth of diesel for different chamber pressures (simulated vs. measured)

measured values, especially for the gas phase. At the beginning of the injection, the gradient of the gas penetration depth deviates slightly from the measured penetration depth. The gradient is higher than in the optical recordings, but decreases as soon as the injection velocity is constant.

Figures 6 and 7 show a comparison of simulation and measurement for the influence of a chamber pressure variation on the mixture formation and the spray penetration depths, respectively. As already observed in the measurements, the simulation shows that the penetration depths of both the liquid phase and the disperse droplet phase decrease with increasing chamber pressure at the same injection rate or injection quantity (depending to a large extent on the rail pressure and the actuation time, however, both almost constant). The higher the relative velocity between the combustion chamber gas and the fuel droplets on one hand, and the higher the density in the combustion chamber (thus the chamber pressure) on the other, the better the diesel fuel

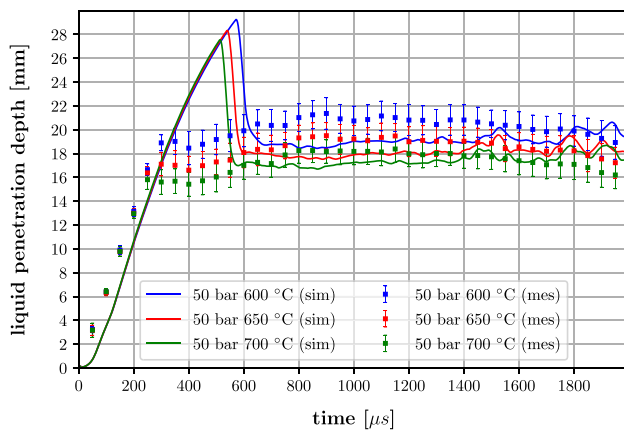


Fig. 8 Liquid penetration depth of diesel for different chamber temperatures (simulated vs. measured)

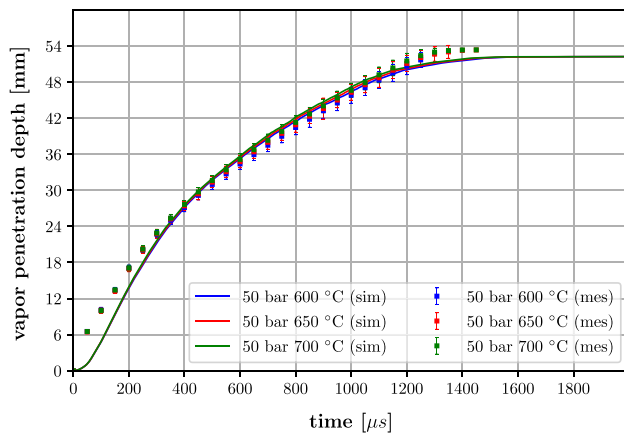


Fig. 9 Vapor penetration depth of diesel for different chamber temperatures (simulated vs. measured)

mixture formation. As a result of the fuel jet entering the combustion chamber, the surrounding air is accelerated. With increasing chamber pressure, the momentum exchange increases, resulting in improved mixture preparation and locally leaner A/F ratios. The jet cone angle increases slightly, while the jet penetration depth decreases. Accordingly, the evaporation rate increases as the chamber pressure rises.

The comparison between the curves of the spray penetration depths over time of the optical measurements and the 3D CFD simulation at varying chamber pressures shows that the penetration depths are largely reproduced correctly. There is a tendency of the simulated penetration depth to lag behind and decrease less than in the experiments. With higher chamber pressure, the difference between

measurement and simulation becomes smaller. Basically, the penetration behavior is particularly dominated by the mixing processes and the momentum exchange with the ambient gas. After the start of injection, the penetration depth of the fuel spray increases linearly until the evaporation rate equals the injection rate. As soon as this equilibrium is reached, the liquid phase of the fuel spray does not penetrate further into the combustion chamber. The increase in penetration depth from the start of injection up to 300 μ s can be mapped very well numerically. The gas phase also fits very well.

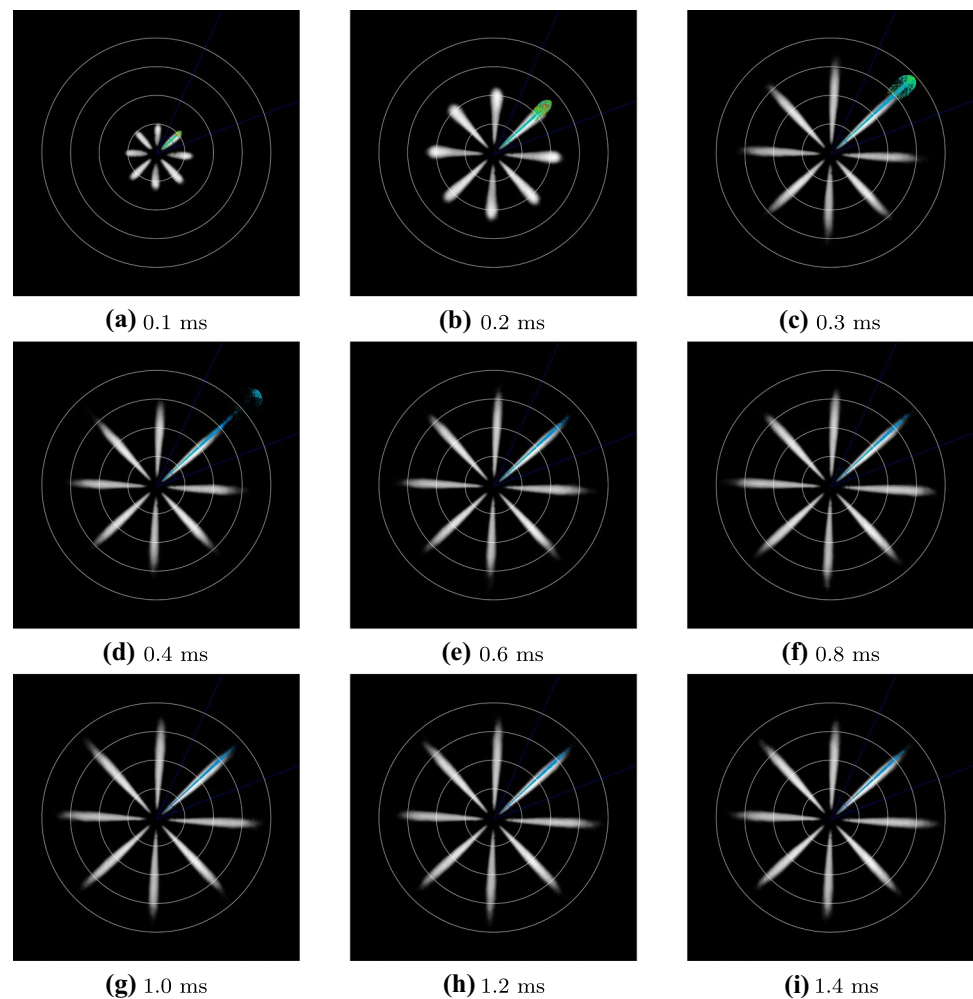
In Figs. 8 and 9, another comparison of penetration depths is displayed; however, this time for a variation of chamber temperature at a constant chamber pressure of 50 bar. The higher the chamber temperature, the faster the evaporation of the droplets and the lower the penetration depth of the liquid phase. This trend can also be found in the simulation results.

When the colder injection spray enters the hot combustion chamber, a heat flow takes place between the combustion chamber gas and the fuel droplets due to the temperature gradient. The temperature of the surrounding gas phase has a decisive influence on the evaporation rate. However, as density decreases with increasing temperature, the momentum exchange is again reduced. The comparison between the simulation and the spray visualization results for the penetration depth with varying gas temperature shows that the progression and the physical phenomena can be reproduced well. However, the differences between the liquid phase penetration depths observed in the experiments are larger for the same temperature steps than those obtained from the simulation. In contrary to the liquid phase, the vapor penetration shows no significant dependency on temperature.

The numerical modeling produces quite good results for the gas phase, which largely coincide with the measurements. The deviation of the gradient of the penetration depth from the experimentally determined curves is due to the slightly different injection patterns during the first 300 microseconds, resulting from the nozzle internal flow simulation.

In summary, it can be stated that the penetration depth is basically a function of injection pressure, combustion chamber temperature, combustion chamber pressure and the spray hole geometry, as well as the fuel properties. Numerical modeling of injection taking into account the internal injector flow and using the Fischer primary decomposition break-up model, yields good results for diesel in terms of liquid and gas phase penetration depth. There is a tendency for the simulated liquid phase penetration depths to slightly underestimate the measured values, both for the pressure and the temperature variation. The curves of the gas phase penetration depth can be reproduced much better compared to

Fig. 10 Intensity-based average images of Mie scattering measurements (white) compared with simulation results (blue) at 80 bar and 600 °C (diesel fuel)



the liquid phase. It should be noted that the calculated results from the optical measurements used here are mean values from 32 individual injections and for all of the spray jets, thus eliminating fluctuations in the penetration depths which might occur in reality. It also needs to be taken into account that the boundary conditions, in particular the results of the nozzle internal flow simulation as input for the *Fischer primary break-up model*, might differ slightly from the real conditions. Still, the simulation settings determined in the present paper (spray parameters, discretisation settings) can be transferred to a subsequent combustion simulation, as the differences in mixture formation are small.

For the three-dimensional evaluation of the spray shape, the simulation results are compared to the optical results from the injection chamber in the following. The operating point with a chamber pressure of 80 bar and a temperature of 600 °C is used as an example. The comparison aims primarily at assessing the development of the spray cone

angle and the penetration depth of the liquid and gaseous phases using intensity-based mean value images, cf. Figs. 10 and 11. It needs to be taken into account that the simulated fuel spray only represents one single spray cone. For optical comparison, the representation of discrete parcels is chosen for the numerically calculated liquid phase. The simulated gas phase is represented with blue isosurfaces. These include all surfaces with a vapour content above 1%.

Both the simulation and the optical images show that immediately after SOI the fuel spray (liquid phase) has a mushroom-like shape at the jet tip and an associated larger jet cone angle, see Fig. 10b, c. When the injection rate and the evaporation rate are in equilibrium, a better correlation between simulation and measurement can be observed. The simulated fuel jet tends to show a smaller jet cone angle, but the core of the injection jet fits very well.

The trace for the gas phase also shows that the numerical modeling can reproduce the actual evaporation behavior, in

Fig. 11 Intensity-based average images of Schlieren measurements (white) compared with simulation results (blue) at 80 bar and 600 °C (diesel fuel)

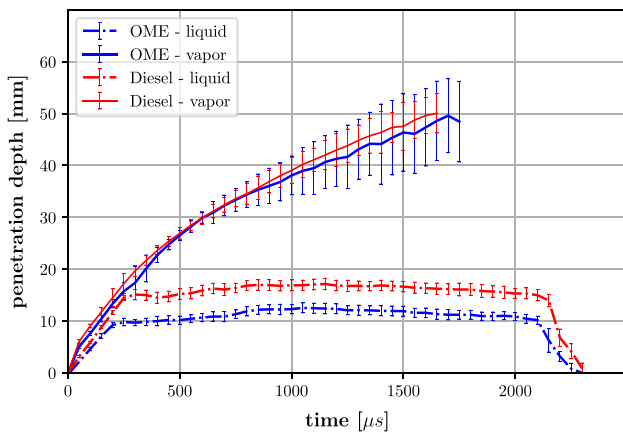
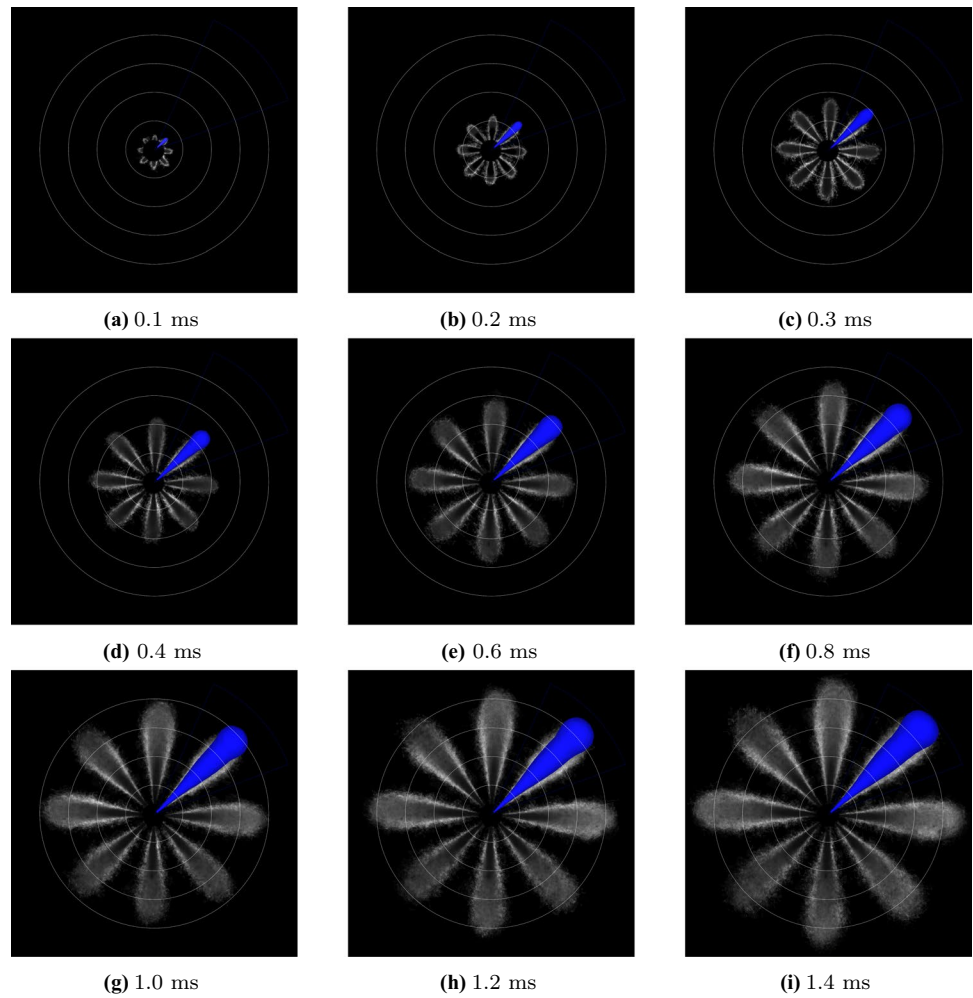


Fig. 12 Liquid and vapor penetration depth diesel vs. OME (measurements) at 80 bar and 600 °C

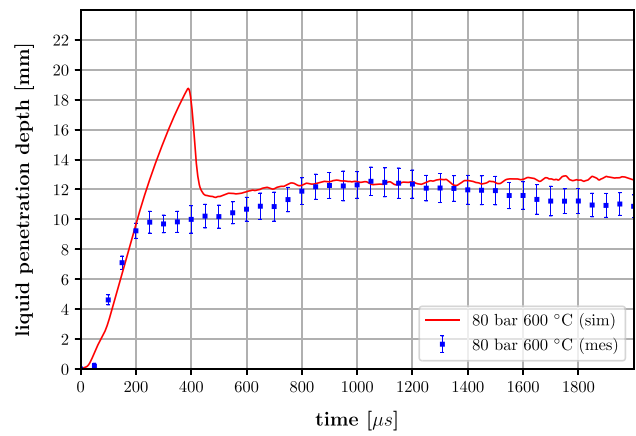


Fig. 13 Liquid penetration depth of OME (simulated vs. measured)

Fig. 14 Intensity-based average images of Mie scattering measurements (white) compared with simulation results (blue) at 80 bar and 600 °C (OME fuel)

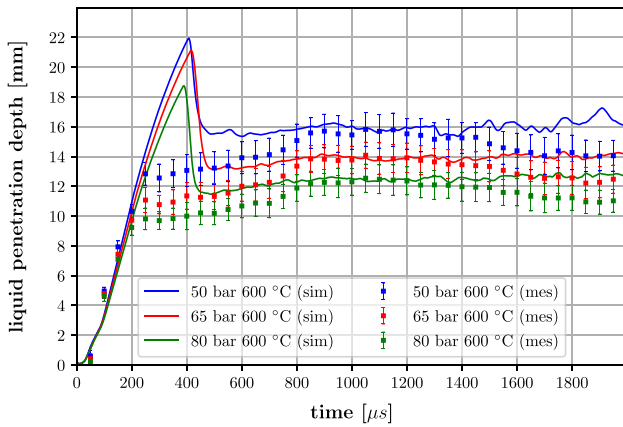
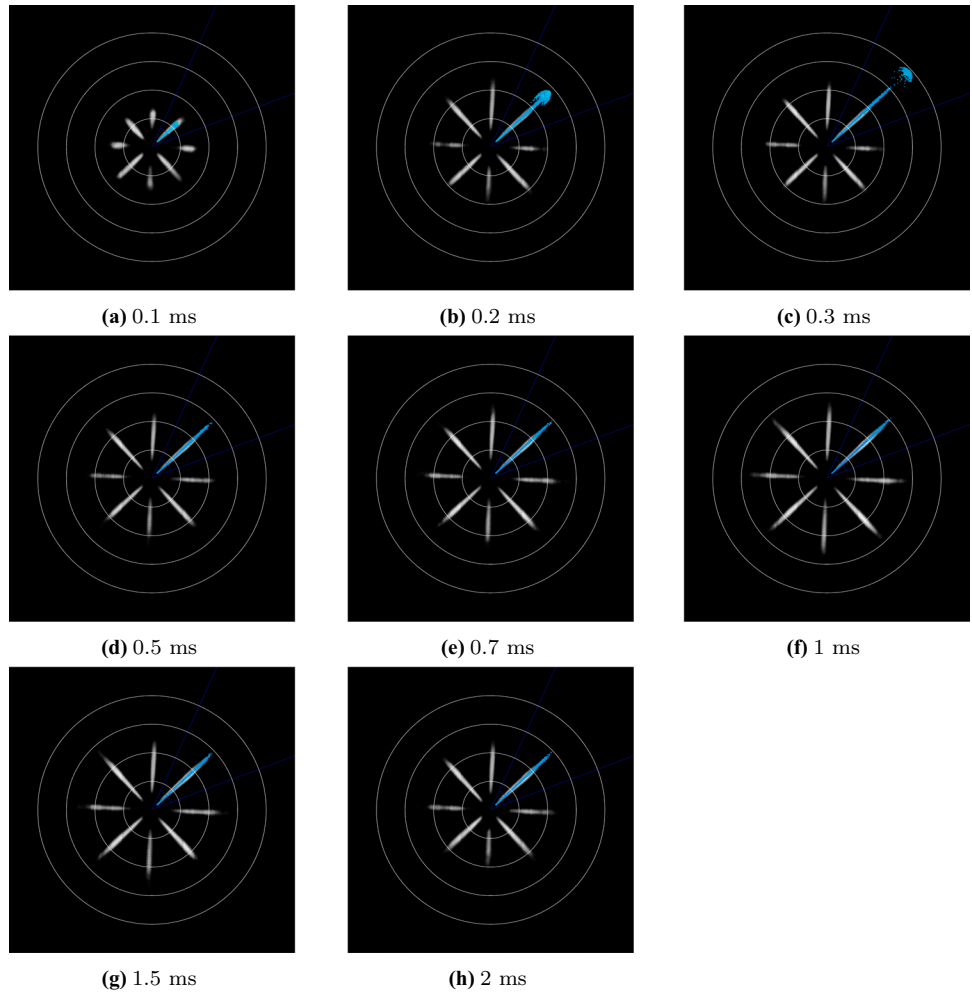


Fig. 15 Liquid penetration depth of OME for different chamber pressures (simulated vs. measured)

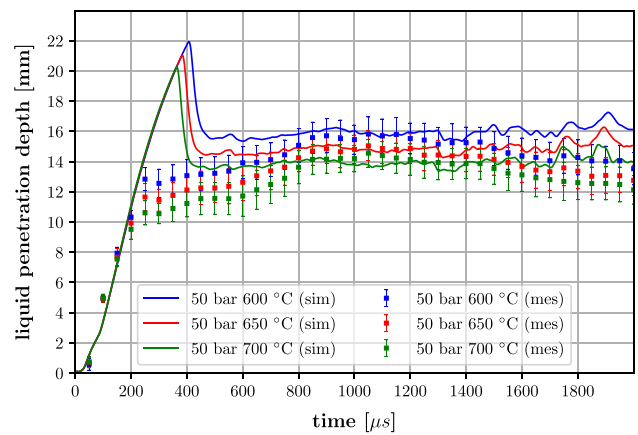


Fig. 16 Liquid penetration depth of OME for different chamber temperatures (simulated vs. measured)

particular the intensity center of gravity. In the boundary areas, it can be seen that the spray cones derived from the optical measurement are slightly larger. However, penetration depths are identical. 1.4 ms after the start of injection, the fuel vapour reaches its maximum penetration depth due to the calculation area selected in the simulation.

3.2 OME spray simulation

For the OME spray simulation and experiments, the same approach as described above for diesel was used. Before evaluating the results, we will first take a look at the

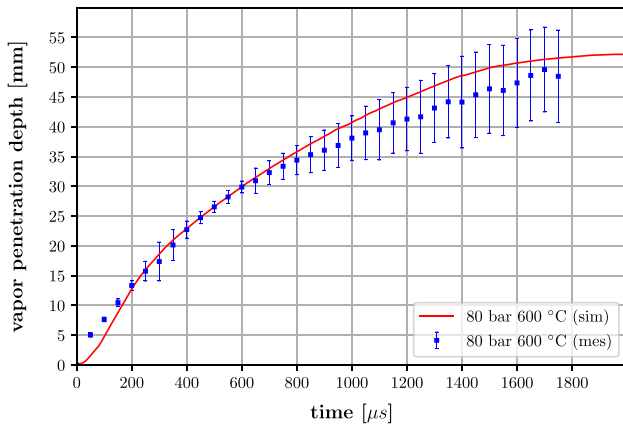


Fig. 17 Vapor penetration depth of OME (simulated vs. measured)

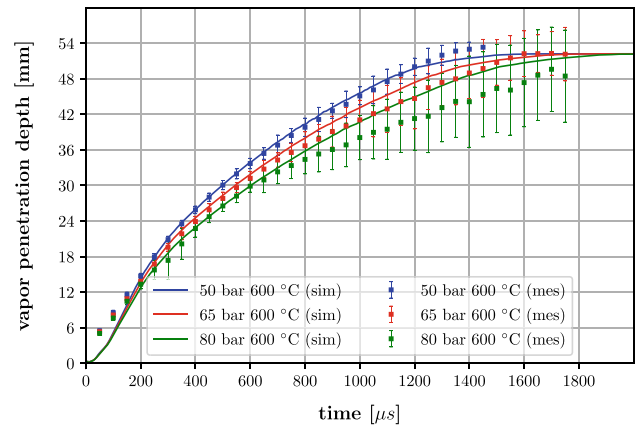


Fig. 19 Vapor penetration depth of OME for different chamber pressures (simulated vs. measured)

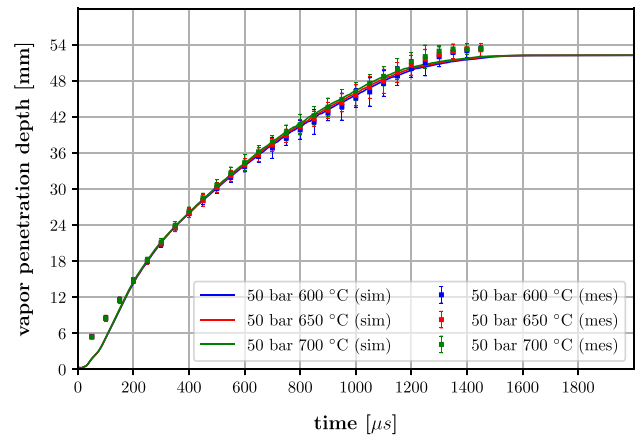
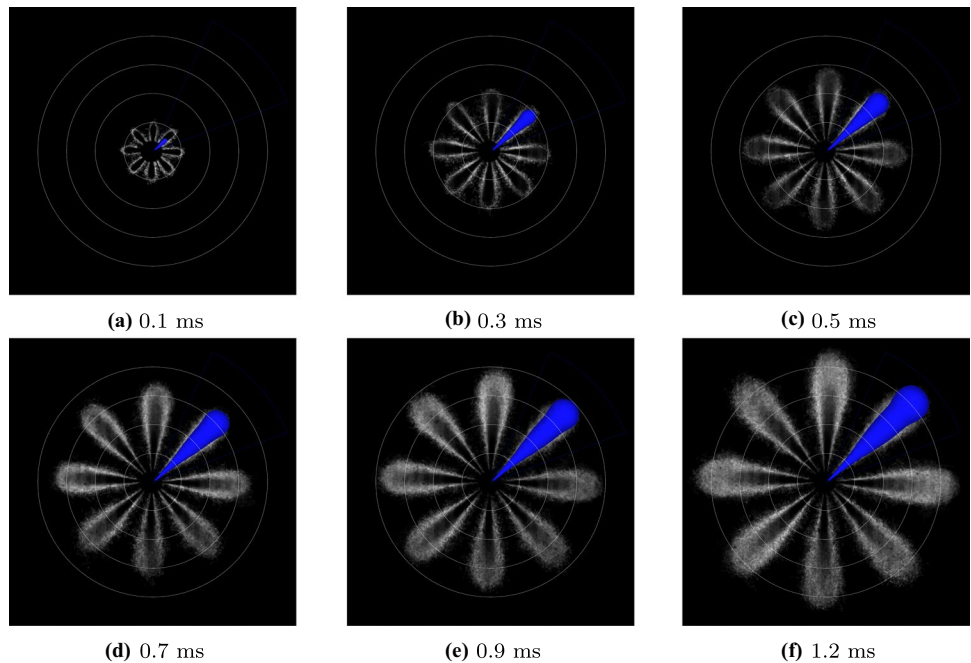


Fig. 20 Vapor penetration depth of OME for different chamber temperatures (simulated vs. measured)

Fig. 18 Intensity-based average images of Schlieren measurements (white) compared with simulation results (blue) at 80 bar and 600 °C (OME fuel)



penetration depths of OME and diesel obtained from the measurement in direct comparison. Figure 12 represents the liquid and the vapor penetration depth as a function of time. From the Schlieren and Mie scattering measurements, it is evident that OME has a significantly reduced liquid penetration depth compared to diesel. The associated faster evaporation results from accelerated droplet decomposition. The penetration depth of the fuel vapor, on the other hand, is almost identically for both fuels in the present case.

As obvious from Fig. 13, the characteristic of the OME injection is reproduced well in the simulation. The decisive factor here is the implementation of the specific substance data of the respective pure fuels (OME3 and OME4). As already described, dedicated measurements were carried out here to determine the temperature-dependent variables, such as density, viscosity, specific heat capacity, etc. (see Table 6).

Since the proportion of OME5 in the mixture used here is almost negligible and no material data are available for OME5, a mixture of 40% OME3 and 60% OME4 is used for the simulation. For validation, the chamber pressure and the chamber temperature have also been varied. The results show good agreement between the simulation and the measurements performed in the high pressure chamber.

Figure 13 shows the liquid penetration depth as a function of time. Similar to the diesel simulation runs, the overshoot for the time interval between 0.2 and 0.5 ms can also be found here. As already explained, this results from the numerical calculation of the penetration depth for which, unlike in the experiment, also very small individual droplets are included in the calculation. Besides, inaccuracies of the primary breakup modeling might contribute to this effect [26, 31]. After about 0.5 ms, the penetration depth approaches a constant value, lying largely within the statistic deviation of the measurement results. Even though the calculations for OME still leave room for improvement in some areas regarding the penetration depth, the difference compared to diesel can be reproduced acceptably.

In Fig. 14, the simulation of a single jet is superimposed on an intensity-based average of the measurements for different time steps. After the initial overshoot, which is again visible through a mushroom-like breakup [Fig. 14(b) and (c)], an acceptable agreement of the simulated injection jet with the measured jet can be detected. However, it is also obvious that model adjustments are still necessary to optimize the injection process, especially at the beginning and at the

end. Nevertheless, the difference between diesel and OME can be reproduced well. The pressure and temperature variations also show quite good agreement between the liquid penetration depth and the corresponding measured values. In Figs. 15 and 16, the penetration depth is again plotted as a function of time.

Looking at the gas phase, it is also visible that the agreement lies within the tolerances of the measurement. In Fig. 17, the gas penetration depth is plotted vs. time; in this case at an internal chamber pressure of 80 bar and a chamber temperature of 600 °C. The gas phase penetration is captured well in the simulation. Hence, it can be concluded that the entrainment of the ambient gas is modeled correctly.

The spray visualization further substantiates this statement. As obvious from Fig. 18, the simulation results coincide very well with the images from the measurement. When varying the pressure in the chamber, the expected effect can also be found.

As with the diesel calculations, an increase in the internal chamber pressure leads to a reduction of the penetration of both the liquid and the gaseous phase of the injected fuel (Figs. 15 and 19). When the temperature is increased, the liquid phase shows a similar change as observed during the pressure variation. Similar to the observations made with Diesel fuel, the gas phase penetration does not change notably at varying chamber temperatures (cf. Figs. 16 and 20).

4 Summary and outlook

Current research activities in the field of synthetic fuels require the development of appropriate numerical models for the injection and combustion of these new fuels to be able to understand and optimize the engine process, and thus exploit the full potential in terms of pollutant and CO₂ emissions. Jet breakup behavior, fuel evaporation and mixture formation play a major role in this context. In the current investigation, the jet breakup behavior of diesel fuel and OME is modeled in 3D CFD for several parameter variations (ambient pressure/temperature and injection pressure) and compared with the results from experiments carried out in a high-pressure chamber. The investigations are carried out using a standard 8-hole diesel injector, without any special adaptations of the nozzle to OME.

To model the primary breakup reliably, the Fischer breakup model has been used for calculating the distribution

of the primary droplets in a single-fluid model based on the results of an internal nozzle flow simulation, thus modeling the region near the nozzle particularly well. The injection rates and valve actuation times in the internal nozzle flow simulation were adapted to the optical measurements to generate the nozzle file underlying the Fischer model.

Furthermore, fluid analyses were carried out to characterize the fuel, as the relevant data were not available from literature. The values obtained from the analysis were used to implement the most important material parameters in the simulation program *AVL FIRETM*. To validate the injection of diesel and OME simulated in a sector model, the experimentally determined data from Schlieren and Mie scattering images were used. The study was carried out for several operating points. The jet penetration behavior of the liquid and gas phases were investigated, as well as the optical appearance of the fuel jet. The optical measurements could be reproduced well by the numerical model for both diesel and OME. In particular, the center of intensity and the penetration depth of the fuel jet could be modeled acceptably. Deviations observed in the liquid phase still require more intensive investigations and could possibly be improved by further optimization of the injector internal flow simulation. Particular attention also needs to be paid to the overshoot at the start of injection and to the deviations in the liquid penetration depth of OME.

In continuation to this study, it is planned to carry out combustion simulations. The results of these simulations will help to judge whether the combination of injection models presented in this paper ensures sufficiently accurate modeling of combustion.

A nozzle flow

Figure 21¹ shows exemplarily some selected results of an injector internal flow simulation, here represented by the volume fraction of the different phases of the fuel (liquid and vaporized) at the beginning of the injection and after about 0.8 ms. The cavitation at the injection hole entrance is well visible in all images and needs to be taken into account in the subsequent modelling by the Fischer model.

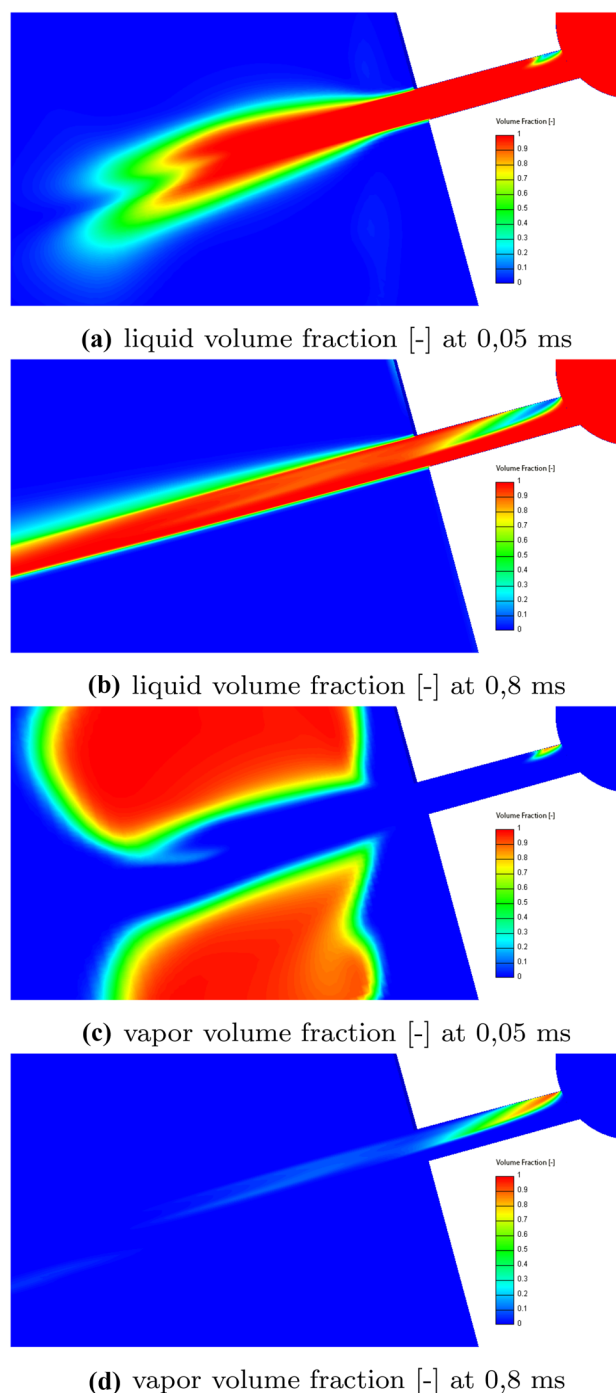


Fig. 21 Volume fraction determined by the injector internal flow simulation at selected time steps

¹ The illustrations are taken from a generic simulation and are intended only as an example of the simulations carried out, since the geometry data are subject to confidentiality and may not be published.

B nozzle file

In Figs. 22 and 23, the structure of the nozzle file is shown. In the header, the plane of the nozzle hole is defined, cf. Fig. 22. The body is divided into two lines per cell and contains the respective flow variables, such as the coordinates in

x, y, z direction, the velocity components u, v, w , as well as the density of the two fuel phases, the turbulent kinetic energy, the dissipation rate, the volume fraction and the size of the cell (see Fig. 23).

Fig. 22 Structure of the nozzle file resulting from the injector internal flow simulation

```

1  FIRE-V 8.2          FMT-SE   0 0
2  FIRE-V 8.2
3
4  8.2 LINES=1 VECTOR OF NOZZLE DIRECTION
5  0.0000E+00, 0.0000E+00, 1.0000E+00
6  8.2 LINES=1 COORDINATES OF ORIFICE CENTER
7  0.0000E+00, 1.0540E-03, -1.6855E-03
8  8.2 LINES=1 NORMAL VECTOR OF ORIFICE PLANE
9  1.0000E-04, 9.7910E-01, -2.0350E-01
10 8.2 LINES=1 SECTOR ANGLE OF NOZZLE CALCULATION[DEG]
11 360
12 8.2 LINES=1 SECTOR ANGLE OF SPRAY CALCULATION[DEG]
13 360
14 8.2 LINES=1 NUMBER OF SYMMETRY PLANES
15 0
16 #8.2 LINES=0 NORMAL VECTOR OF SYMMETRY PLANES
17 8.2 LINES=1 LIQUID MASS IDENTIFIER
18 1
19 8.2 LINES=1 GDI-MODE
20 0
21 8.2 LINES=1 TAKE MASS FLOW FROM SPRAY FILE
22 0
23 8.2 LINES=1 NUMBER OF BLOBS
24 0
25 8.2 LINES=1 NUMBER OF DATASETS
26 221
27 8.2 LINES=221 TIME OF DATASETS
28 0.0000E+00
29 1.0000E-05
30 2.0000E-05
31 3.0000E-05
32 4.0000E-05
33 5.0000E-05

```

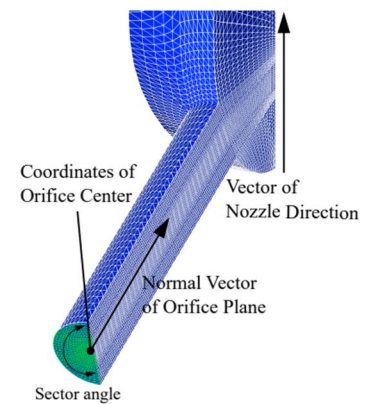


Fig. 23 Body of the nozzle file containing the simulated flow variables and assigning them to the polar grid

```

245 2.1700E-03
246 2.1800E-03
247 2.1900E-03
248 2.2000E-03
249 8.2 LINES=1 NUMBER OF FACES
250 3054
251 8.2 LINES=1349868 FACE VALUES
252 -4.220E-05 1.063E-03-1.644E-03 6.800E-09 1.426E-06-3.015E-07
253 7.993E-03 9.156E-17 6.098E-07 1.510E-12 8.982E-14 8.192E-07
254 -4.221E-05 1.063E-03-1.644E-03-3.799E-09 7.088E-07-1.425E-07
255 7.993E-03 1.970E-17 4.648E-07 9.665E-13 3.672E-14 8.192E-07
256 -4.022E-05 1.063E-03-1.642E-03 5.537E-09 7.244E-07-1.566E-07
257 7.993E-03 1.808E-17 4.268E-07 1.646E-12 3.372E-14 8.192E-07

```

C substance data

See Figs. 24, 25, 26, 27, 28, 29, 30, 31.

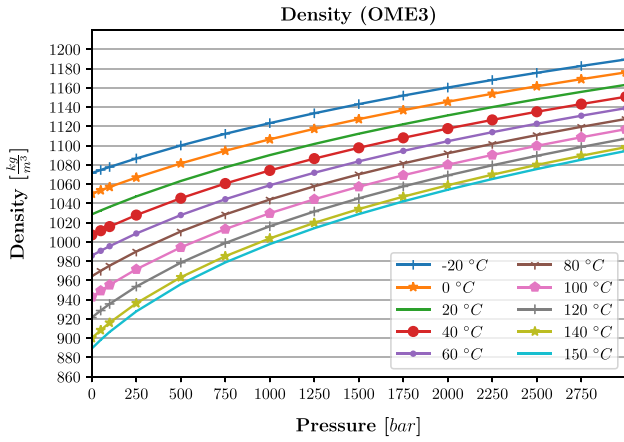


Fig. 24 Density (OME3)

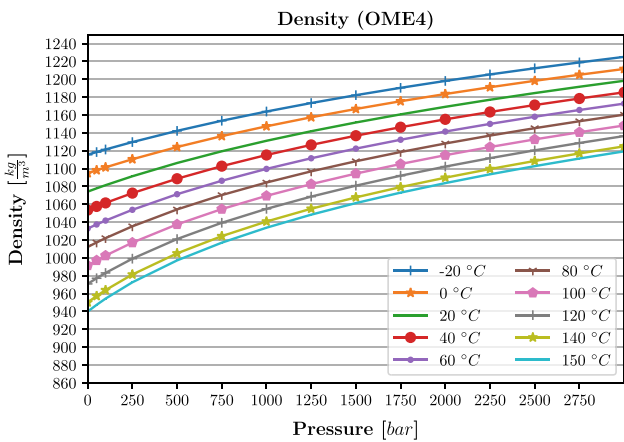


Fig. 25 Density (OME4)

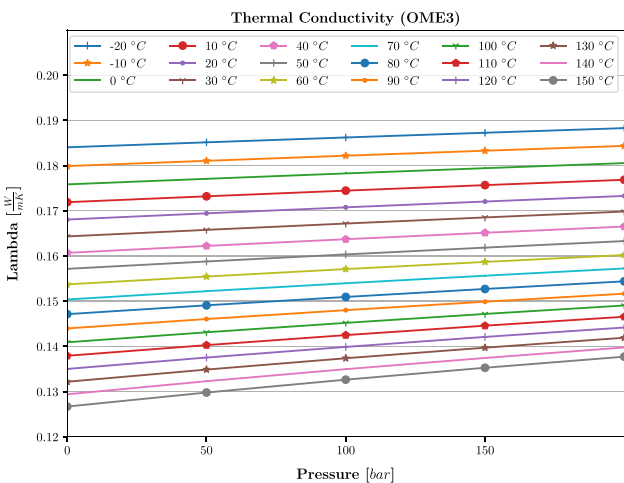


Fig. 26 Thermal conductivity (OME3)

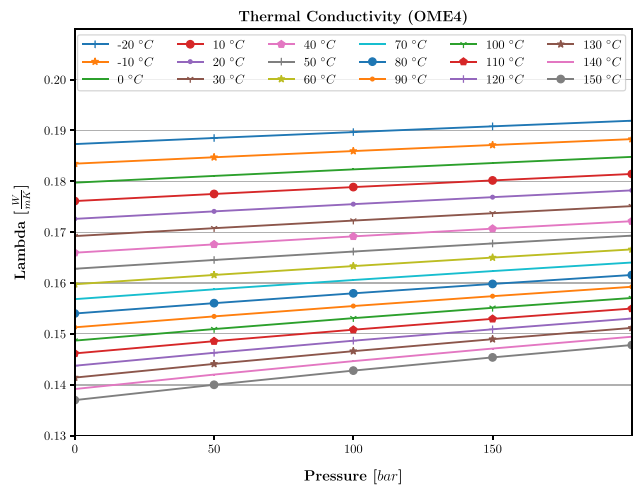


Fig. 27 Thermal conductivity (OME4)

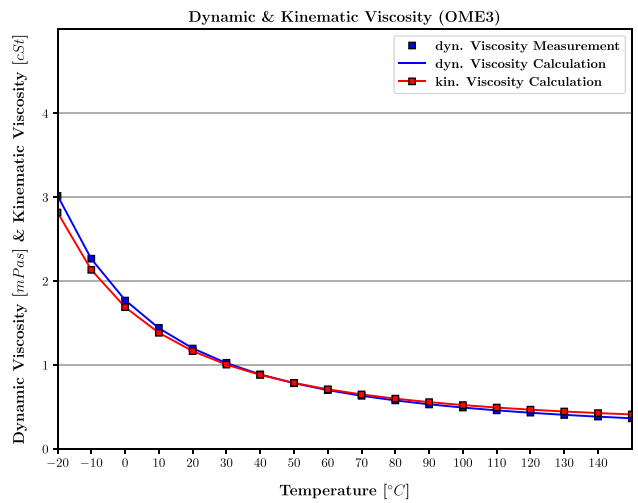


Fig. 28 Dynamic & kinematic viscosity (OME3)

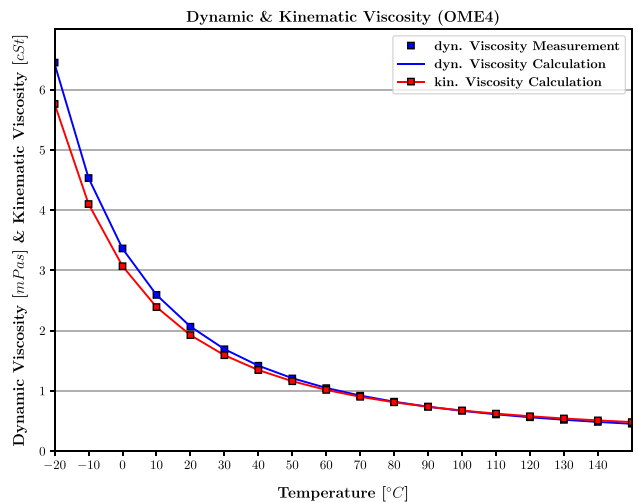


Fig. 29 Dynamic & kinematic viscosity (OME4)

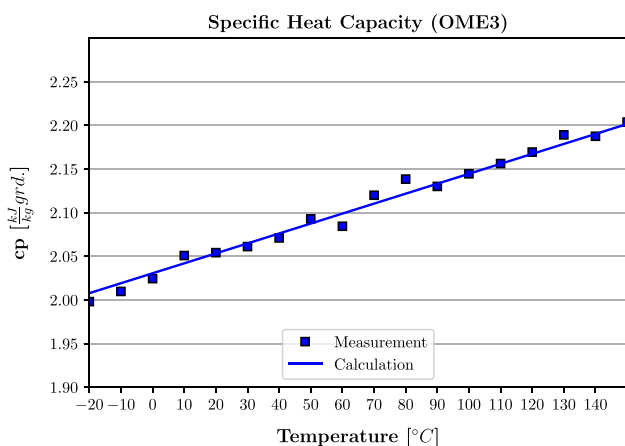


Fig. 30 Specific heat capacity (OME3)

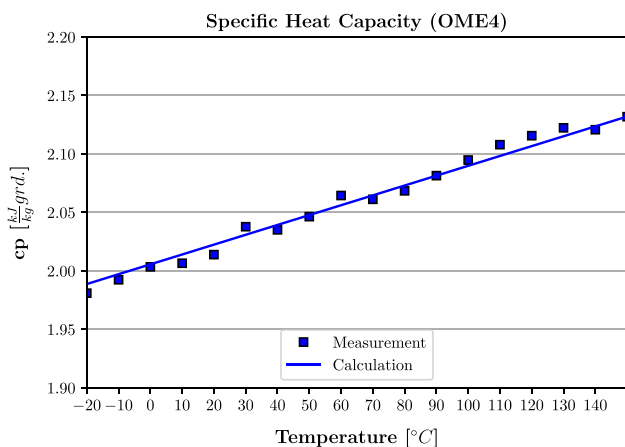


Fig. 31 Specific heat capacity (OME4)

Acknowledgements The work presented here was carried out within the framework of the project “E2Fuels” (funding code: 19I18008F), funded by the German Federal Ministry of Economic Affairs and Climate Action. The authors would like to express their gratitude for this funding. The optical investigations were carried out at the Institute of Engineering Thermodynamics of Erlangen University (Germany) as a subcontractor.

Funding Open Access funding enabled and organized by Projekt DEAL.

Open Access This article is licensed under a Creative Commons Attribution 4.0 International License, which permits use, sharing, adaptation, distribution and reproduction in any medium or format, as long as you give appropriate credit to the original author(s) and the source, provide a link to the Creative Commons licence, and indicate if changes were made. The images or other third party material in this article are included in the article's Creative Commons licence, unless indicated otherwise in a credit line to the material. If material is not included in the article's Creative Commons licence and your intended use is not permitted by statutory regulation or exceeds the permitted use, you will

need to obtain permission directly from the copyright holder. To view a copy of this licence, visit <http://creativecommons.org/licenses/by/4.0/>.

References

- Cai, L., Jacobs, S., Langer, R., vom Lehn, F., Pitsch, H.: Auto-ignition of oxymethylene ethers (OMEn, $n = 2-4$) as promising synthetic e-fuels from renewable electricity: shock tube experiments and automatic mechanism generation. *Fuel* **264**, 116711 (2020). <https://doi.org/10.1016/j.fuel.2019.116711>
- Pöllmann, S., Härtl, M., Wachtmeister, G.: Potential of miller timing with synthetic diesel fuels on a single cylinder heavy-duty engine. *Int J Engine Res* (2021). <https://doi.org/10.1177/14680874211043649>
- Damyantov, A., Hofmann, P., Geringer, B., Schwaiger, N., Pichler, T., Siebenhofer, M.: Biogenous ethers: production and operation in a diesel engine. *Automot Engine Technol* **3**(1), 69–82 (2018). <https://doi.org/10.1007/s41104-018-0028-x>
- Liu, H., Wang, Z., Wang, J., He, X., Zheng, Y., Tang, Q., Wang, J.: Performance, combustion and emission characteristics of a diesel engine fueled with polyoxymethylene dimethyl ethers (PODE3-4)/ diesel blends. *Energy* **88**, 793–800 (2015). <https://doi.org/10.1016/j.energy.2015.05.088>
- Lumpp, B., Rothe, D., Pastötter, C., Lämmermann, R., Jacob, E.: Oxymethylenether als Dieselkraftstoffzusätze der Zukunft. *MTZ Motortech Z* **72**(3), 198–203 (2011). <https://doi.org/10.1365/s35146-011-0049-8>
- Härtl, M., Gaukel, K., Pélerin, D., Wachtmeister, G.: Oxymethylene ether as potentially CO₂-neutral fuel for clean diesel engines part 1: engine testing. *MTZ Worldwide* **78**(2), 52–59 (2017). <https://doi.org/10.1007/s38313-016-0163-6>
- Richter, G., Zellbeck, H.: Oxymethylene ethers as an alternative for passenger car diesel engines. *MTZ Worldwide* **78**(12), 60–67 (2017). <https://doi.org/10.1007/s38313-017-0126-6>
- Holzer, A., Guenther, M.: Investigation of the emission reduction potential of HVO-OME fuel blends in a single-cylinder diesel engine. *SAE Technical Paper* 2021–01–0556. SAE International (2021). <https://doi.org/10.4271/2021-01-0556>
- Jacob, E., Stark, M., Härtl, M., Wachtmeister, G.: C1-Oxygenate als zukünftige Kraftstoffe. (2019) In: *Proceedings / Tschöke, H., Marohn, R. (eds) 11. Tagung Einspritzung und Kraftstoffe 2018*. https://doi.org/10.1007/978-3-658-23181-1_2
- Jacob, E.: C-1 Oxygenate als nachhaltige Kraftstoffe und deren günstige Eigenschaften. (2019) In: *Maus, W. (eds) Zukünftige Kraftstoffe*. *ATZ/MTZ-Fachbuch*. https://doi.org/10.1007/978-3-662-58006-6_9
- Oestreich, D.: Prozessentwicklung zur Gewinnung von Oxymethylenethern (OME) aus Methanol und Formaldehyd. PhD thesis. Karlsruhe Institut für Technologie (KIT), (2017)
- Lautenschütz, L., Oestreich, D., Seidenspinner, P., Arnold, U., Dinjus, E., Sauer, J.: Physicochemical properties and fuel characteristics of oxymethylene dialkyl ethers. *Fuel* (173), 129–137 (2016). <https://doi.org/10.1016/j.fuel.2016.01.060>
- Kraftstoffe - Dieselkraftstoff - Anforderungen und Prüfverfahren. Norm. EN 590:2013+A1:2017
- Peter, A., Siewert, B., Riess, S., Strauss, L., Pastötter, C., Wensing, M.: Mixture formation analysis of polyoxymethylenether injection. *Atomization and Sprays* **30**(11), 843–859 (2020). <https://doi.org/10.1615/AtomizSpr.2020035250>
- Colin, O., Benkenida, A.: The 3-zones extended Coherent flame model (Ecfm3z) for computing premixed/diffusion combustion. *Oil Gas Sci Technol* **59**, 593–609 (2004). <https://doi.org/10.2516/ogst:2004043>

16. Hänel, D.: Molekulare Gasdynamik: Einführung in die kinetische Theorie der Gase und LatticeBoltzmann-Methoden. Springer-Verlag Berlin Heidelberg (2004). <https://doi.org/10.1007/3-540-35047-0>
17. Baumgarten, C.: Mixture Formation in Internal Combustion Engines. Springer-Verlag Berlin Heidelberg (2006). <https://doi.org/10.1007/3-540-30836-9>
18. Schiller, L., Naumann, Z.: A Drag Coefficient Correlation. VDI Zeitung **77**, 318–320 (1935)
19. Dukowicz, J.K.: Quasi-steady droplet change in the presence of convection. Los Alamos Scientific Lab., NM (USA) (1979). <https://doi.org/10.2172/6012968>
20. Möller, S., Dutzler, G.K., Priesching, P., Pastor, J.V., Micó, C.: Multi-Component Modeling of Diesel Fuel for Injection and Combustion Simulation. SAE Technical Paper 2013-24-0007. SAE International (2013). <https://doi.org/10.4271/2013-24-0007>
21. Pham, V., Choi, J., Rho, B., Kim, J., Park, K., Park, S., Le, V., Lee, W.: A Numerical Study on the Combustion Process and Emission Characteristics of a Natural Gas-Diesel Dual-Fuel Marine Engine at Full Load. Energies **14**(5), (2021). <https://doi.org/10.3390/en14051342>
22. Abramzon, B., Sirignano, W.A.: Droplet vaporization model for spray combustion calculations. Int J Heat Mass Transfer **32**(9), 1605–1618 (1988). [https://doi.org/10.1016/0017-9310\(89\)90043-4](https://doi.org/10.1016/0017-9310(89)90043-4)
23. Brenn, G., Deviprasath, L.J., Durst, F.: Computations and experiments on the evaporation of multi-component droplets. In: Proceedings/9th Int. Conf. Liquid Atomiz. Spray Syst. (ILASS) (2003)
24. Fink, C.: A Multi-Component Evaporation Model for the 3D CFD Code FIRE 8 - Development and Validation with Experimental Data. PhD thesis. TU Graz (2005)
25. AVL LIST GmbH. AVL FIRE v2019 manual (2019)
26. Fischer, F.: Primary breakup model considering the spray core development. PhD thesis. TU Darmstadt, (2011). ISBN:9783844003833
27. Fischer, F., Heine, B., Tropea, C.: Primary breakup model considering spray core development. In: Proceedings / 23rd Int. Conf. Liquid Atomiz. Spray Syst. (ILASS) (2010).
28. Beale, J.C., Reitz, R.D. Modeling spray atomization with the Kelvin-Helmholtz / RayleighTaylor hybrid model. Atomization and Sprays **9**(6) (1999). <https://doi.org/10.1615/AtomizSpr.v9.i6.40>
29. Yaws, C.L.: The Yaws handbook of physical properties for hydrocarbons and chemicals: Physical properties for more than 54,000 organic and inorganic chemical compounds, coverage for C1 to C100 organics and Ac to Zr inorganics. Elsevier Science (2015)
30. Fechter, M.H.H., Haspel, P., Hasse, C., Braeuer, A. S.: Vapor pressures and latent heats of vaporization of Poly(oxymethylene) Dimethyl Ethers (OME3 and OME4) up to the vicinity of the critical temperature. Fuel **303**, 121274 (2021). <https://doi.org/10.1016/j.fuel.2021.121274>
31. Spiekermann, P., Jerzembeck, S., Felsch, C., Vogel, S., Gauding, M., Peters, N.: Experimental data and numerical simulation of common-rail ethanol sprays at diesel engine-like conditions. Atomization and Sprays **19**(4), 357–386 (2009). <https://doi.org/10.1615/AtomizSpr.v19.i4.40>

Publisher's Note Springer Nature remains neutral with regard to jurisdictional claims in published maps and institutional affiliations.